One-step microwave-assisted synthesis of metal-free heteroatom-doped carbon catalyst for H$_2$O$_2$ electrosynthesis

Milena Šetka [a,c,*], Albert Behner [a], Roman Bleha [b], Milutin Smiljanić [c], Nejc Hodnik [c], Miroslav Šoóš [a]

[a] *Department of Chemical Engineering, University of Chemistry and Technology Prague, Technická 3, 166 28 .Prague 6, Czech Republic*
[b] *Department of Carbohydrates and Cereals, University of Chemistry and Technology Prague, Technická 3, 166 28 Prague 6, Czech Republic*
[c] *Department of Materials Chemistry, National Institute of Chemistry, Hajdrihova 19, 1000 Ljubljana, Slovenia*

ARTICLE INFO

ABSTRACT

This study reports on a one-step conversion of polyaniline into a metal-free heteroatom-doped carbon electrocatalyst through microwave heating. A high surface area carbonaceous structure forms after a total synthesis time of only 140 s, with the presence of nitrogen and oxygen functional groups, as confirmed by thorough spectroscopic analysis. This catalyst exhibits high activity (onset potential of 0.73 V vs. RHE), selectivity (82 %), and stability (over a 7.5-hour test period) for the electrochemical oxygen reduction reaction towards hydrogen peroxide in alkaline media. Microwave synthesis reduces heating time by 29-fold and energy consumption by 77-fold, while producing materials with high electrocatalytic efficiency comparable to those conventionally prepared at 700°C. The microwave and the conventionally synthesized heteroatom-doped carbon catalysts show similar electrochemical performances, which can be attributed to the presence of nearly identical nitrogen functional groups and surface area in the two samples. In contrast, the microwave and conventionally synthesized samples exhibit significant variations in their oxygen functional groups. These results suggest that nitrogen functional groups are the main active sites for alkaline hydrogen peroxide formation, while oxygen functional groups play a minor role in the catalytic activity. Our work brings a solid contribution to the debate regarding the active centers for hydrogen peroxide formation.

1. Introduction

Hydrogen peroxide (H$_2$O$_2$) ranks among the top 100 most significant chemicals, finding extensive use across various chemical and medical end-user industries including paper and pulp bleaching, water treatment, food processing, electronics, and disinfection in medical and pharmaceutical sectors. Electrochemical oxygen reduction reaction (ORR) via a two-electron (2e$^-$) process presents a sustainable route for on-site and small-scale production of H$_2$O$_2$ compared to the industrial anthraquinone process [1–3]. The quest for high selectivity, activity, and stability of electrocatalysts has led to the exploration of noble-metal-based catalysts or their alloys, notably Pt, Pd, Au, Pt–Hg, and Au–Pd [1,4,5]. However, their high cost, toxicity, and scarcity hinder commercial applications. Moreover, the long-term stability of noble and transition metal-based catalysts remains a concern due to the potential leaching of unstable metal sites, which could lead to a decline in ORR activity and affect performance in various electrochemical devices, including proton exchange membrane fuel cells, H₂O₂ fuel cells and electrolyzers [6–9].

In response to these challenges, metal-free carbon-based catalysts, particularly nitrogen-doped carbon (N–C), have emerged as promising alternatives due to their cost-effectiveness, abundance, and non-toxic nature [10–14]. N–C catalysts have demonstrated high efficacy for ORR to H$_2$O$_2$ in alkaline media, with tunable electronic properties resulting from heteroatom doping and intrinsic defects [5,15]. Incorporating nitrogen into the carbon framework modifies electron distribution, enhancing conductivity and electron transfer during ORR. Additionally, the formation of nitrogen functional groups, such as pyridinic, pyrrolic, and graphitic nitrogen, can increase selectivity for either the 2e$^-$ (producing H$_2$O$_2$) or 4e$^-$ (producing H$_2$O) ORR pathway. However, the literature still lacks a clear agreement on the specific roles of individual nitrogen sites in catalyzing ORR to H$_2$O$_2$ or H$_2$O [4,15,16].

Synthesis methods and applied conditions, including precursor selection, temperature, time, and gas environment, play crucial roles in

the tailoring of key structural properties in the N–C catalysts. Various synthesis methods for N–C catalysts have been studied, including conventional pyrolysis [16,17], hydrothermal synthesis [18], chemical vapor deposition [19], plasma treatments [20], and mechanochemical approaches [21]. While each method offers unique advantages depending on the desired properties and application requirements of the N–C material, they all have in common a long preparation time, often extending over several hours.

Microwave-assisted heating has emerged as a promising sustainable approach for the preparation and modification of various types of carbon-based materials [22–25]. This method offers faster heating, higher energy efficiency, and the potential for nanostructure formation with distinct morphological or structural properties due to direct interaction between chemical precursors and microwave (MW) radiation. Previous studies have mainly used MW heating to synthesize metal-containing electrocatalysts supported on substrates like graphene, carbon nanotubes, or CONV-prepared carbonaceous structures [26,27]. In many cases, the synthesis of porous carbon structures has been performed using MW heating in aqueous solutions [28,29]. When precursors have been directly subjected to MW irradiation in the solid phase, MW susceptors, such as carbon felts, graphite, activated carbon, or metal precursors, have been added to the synthesis to facilitate the process [26,30–32]. However, our synthesis approach is distinct as it focuses on the direct synthesis of metal-free N–C catalysts for the ORR, conducted in the solid phase without the use of MW susceptors.

This study introduces polyaniline (PANI) as a nitrogen-enriched precursor for the direct formation of N–C structures via MW heating, with the synthesis carried out in the solid state. Previous literature has utilized PANI for synthesizing metal-doped or bare N–C catalysts under CONV heating conditions, although with extended reaction durations (3-6 hours) and high energy consumption (reaction temperature of 600-900°C) [33–35]. This study investigates the feasibility of using MW heating as a more sustainable approach for synthesizing metal-free N–C catalysts with enhanced activity, selectivity, and stability for H_2O_2 electrosynthesis. The primary goal of this work is to compare the structural differences and ORR performance of materials produced through MW heating (MW-heated samples) with those synthesized via CONV heating (CONV-heated samples). We thoroughly examine the chemical composition in MW- and CONV-heated samples using Fourier-transform infrared spectroscopy (FTIR), X-ray photoelectron spectroscopy (XPS), and Raman spectroscopy. Additionally, we also provide new insights into the identification of active sites for H_2O_2 production in alkaline media of N–C catalysts.

2. Material and methods

2.1. Chemicals

Aniline (>99.5 %) and ammonium persulfate (>98 %) were purchased from Sigma Aldrich. Potassium hydroxide (KOH, >85 %) and hydrochloric acid (HCl, 35 %) were obtained from PENTA. All chemicals were used as received without further purification. Millipore water was used throughout the study for all synthesis and washing processes.

2.2. Synthesis of PANI samples

The PANI samples were synthesized using a chemical oxidative polymerization reaction according to the modified procedure from the literature [36]. Aniline (5 ml) was dissolved in the solution of hydrochloric acid (50 ml of 1M HCl) and stirred for 30 min. In the next step, the solution of ammonium persulfate (195 ml with a concentration of 0.28 mol/L) was added at a rate of 5 ml/min, and the reaction mixture was stirred (500 RPM) for 4 hours. The reaction was carried out at a temperature of ~4°C. The suspension of PANI aggregates was left for overnight precipitation. The final PANI material, in the form of pellets, was produced using vacuum filtration. This method ensures samples

with uniform shapes and dimensions, which are essential for reproducible microwave heating. After separation, the samples were dried at 80°C and a pressure of 200 mbar for 24 hours.

2.3. Carbonization of PANI samples by CONV heating

PANI samples, weighing 1 g, were CONV heated in covered annealing crucibles to temperatures of 450, 500, 600, 700, and 800°C. During this temperature range, the conversion of PANI to N–C structures took place [37]. A heating rate of 10°C/min was applied, and samples were maintained at the target temperature for 1 minute. Subsequently, heating was stopped, allowing samples to naturally cool to 25°C for 4 to 8 hours. Initially, the air was present in the crucibles, but since the crucibles were closed, the gases released during the decomposition of PANI, such as CO, CO_2, and NO_2, could be exchanged with the air, preventing combustion of the precursor at high temperatures [38].

2.4. Carbonization of PANI samples by MW heating

The PANI samples underwent heating using MW irradiation in a household oven (SAMSUNG MS23F301TAS/EO) with a maximum output power of 800 W. In all experiments, the dimensions and mass (1 g) of the samples were consistently maintained. The sample was placed in an uncovered quartz crucible within an air environment, with the crucible centrally positioned in the MW oven and rotating continuously throughout the synthesis process. This approach ensured the establishment of repeatable conditions. The input power of MW irradiation and time were controlled during MW-assisted carbonization. After exploring various power and time conditions, optimal parameters were determined to be a power of 450 W and exposure times of 70, 140, and 210 s. After the completion of MW heating, the material cooled for 2 minutes before storage and subsequent characterization. The temperature data during MW carbonization are not included here, as they are beyond the scope of this study, which primarily aims to compare the chemical composition resulting from CONV and MW carbonization of PANI samples. Moreover, measuring the temperature precisely during MW heating presents challenges due to localized heating.

2.5. Spectroscopic analysis

The FTIR analysis was recorded using a Thermo Fisher Nicolet 6700 FT-IR spectrometer in the range of 400-4000 cm^{-1}. Samples for FTIR measurements were prepared by compressing CONV heated–samples or MW heated–samples with potassium bromide (KBr) to form pellets. XPS analysis was conducted using ESCA Probe P (Omicron Nanotechnology) with an AlKα monochromator (1486.7 eV). Survey spectra were recorded to identify chemical elements in the N–C–samples with pass energy of 50 eV and step size of 0.4 eV. High-resolution spectra of carbon (C 1s), nitrogen (N 1s), and oxygen (O 1s) were collected to determine the type of functional groups in the synthesized materials. CasaXPS Version 2.3.24 software was utilized for data analysis, with spectra calibrated by the C–C peak at 284.4 eV. Shirley-type background correction and Gaussian: Lorentzian sum (G: Lsum) fitting function (with 0.3 G: Lsum) were applied. The full width at half-maximum (FWHM) was set to 1.0-1.5 eV for deconvoluted C 1s and N 1s peaks, and 1.0-2.0 eV for O 1s peaks. Raman spectra were obtained using a DXR Raman Microscope (Thermo Scientific) in the range of 50-3550 cm^{-1}. A laser with a wavelength of 532 nm and power of 0.3 mW served as the excitation source, with a grating of 900 lines/mm, 25 μm slit aperture, and 50x magnification objective utilized.

2.6. N_2 and CO_2 adsorption measurements

The N_2 and CO_2 adsorption measurements were performed using Quantachrome Nova 2200e. Before the analysis, the samples were degassed under the vacuum at the temperature of 150°C for 6 hours. The

N_2 and CO_2 adsorption isotherms were recorded at a temperature of 77 K and 273.15 K, respectively. The adsorbed volume of the gas was taken for calculations at a pressure of 1 bar.

2.7. Electrochemical ORR measurements

The ORR activity of MW and CONV-heated samples were investigated by cyclic voltammetry (CV) and linear sweep voltammetry (LSV) in the alkaline media (0.1 M KOH) controlled by Bio-Logic SAS (SP-300-240) potentiostat. All electrochemical experiments were performed in the Teflon cell to avoid contamination coming from glass corrosion in contact with alkaline electrolytes. The experiments used a setup with three electrodes: a rotating ring-disk electrode (RRDE from Pine) with a platinum ring (geometric area ($A_{geom.}$) of 0.110 cm^2) and a glassy carbon disk ($A_{geom.}$ of 0.196 cm^2), a graphite rod as the counter electrode, and RHE as the reference electrode. The working electrode was prepared by drop-casting of 10 μl of ink suspension containing 4 mg of catalyst, 800 μl of ethanol, 150 μl of water, and 50 μl of Nafion solution. This resulted in a catalyst loading of 0.2 mg cm^{-2}. Before conducting the ORR measurement, both the working electrode and Pt ring electrode of the RRDE underwent electrochemical cleaning. This involved continuous CV scanning in Ar-saturated 0.1 M KOH from 0.05 to 0.8 V vs. RHE at a scan rate of 500 mV s^{-1} and a rotation speed of 1600 rpm for 50 cycles. After, the background and ORR measurements were performed at the scan rate of 10 mV s^{-1} with the rotation of 1600 rpm in the electrolyte solution saturated with Ar or O_2 for 15 min before each test, respectively. The potential of the Pt ring electrode was set to 1.2 V. The faradaic ORR current from the disk electrode was determined by subtracting the corresponding background current.

The H_2O_2 selectivity was calculated based on the following equation:

$$H_2O_2 \ (\%) = 200*(I_{ring}/N)/((I_{ring}/N)+I_{disk}))$$

where I_{ring} is the ring current, I_{disk} is the disk current and N is the collection efficiency with a value of 0.266 (experimentally determined using 0.01 M $K_3Fe(CN)_6$ + 0.1 M KNO_3 solution mixture).

3. Results and discussion

3.1. FTIR analysis of carbonized PANI samples

FTIR spectroscopy was used to examine the structural modifications induced by MW and CONV heating in the PANI samples. The studied MW- and CONV-heated samples were labeled as C-W-t or C-T-t, respectively, where W represents the applied MW power in watts, T indicates the applied CONV temperature in degrees Celsius, and t denotes the total heating time in seconds. Fig. 1 displays the FTIR spectra (2500-500 cm^{-1}) of bare PANI, alongside samples showing the highest spectral similarities after MW- and CONV-carbonization. Specifically, samples heated with MW power of 450 W for 70 s (C-450W-70s) or 140 s (C-450W-140s) showed the closest match with CONV-heated ones at 450°C (C-450°C-2610s) and 700°C (C-700°C-4110s) among investigated temperatures (see **Fig. S1** for other temperatures), respectively. Results suggested a mild carbonization level in C-450W-70s samples, such as at a lower temperature (e.g., 450°C), while C-450W-140s samples may reach more moderate temperatures (e.g., 700°C) during MW treatment. However, extending MW heating to 210 s resulted in a non-uniform chemical composition for the C-450W-210s sample. Therefore, this sample will not be further analyzed here. However, detailed information about the distinct chemical structures of C-450W-210s can be found in the Supplementary Data.

To identify the chemical composition induced by MW- and CONV-heating under mild and moderate conditions in PANI, we analyzed changes in the FTIR spectra. The detected FTIR bands of bare PANI samples (as detailed in Table 1) corresponded to characteristic peaks described in previous studies [39–42]. The FTIR analysis confirmed the
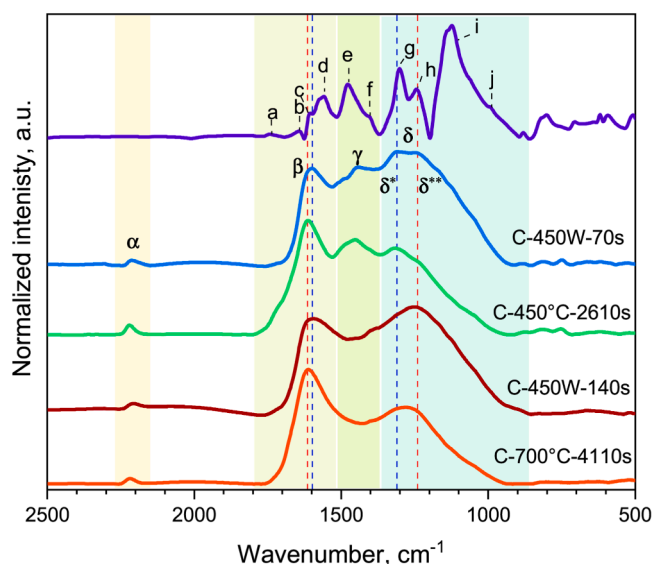

Fig. 1. FTIR spectra of bare PANI, along with MW- and CONV-heated samples, show the highest spectral similarities. The comparison was made between C-450W-70s and C-450°C-2610s samples and between C-450W-140s and C-700°C-4110s samples.

Table 1
Summary of the characteristic FTIR bands observed in bare PANI and MW- and CONV- N–C samples. The studied samples are labeled in the table as follows: C-450W-70s (A), C-450°C-2610s (B), C-450W-140s (C), and C-700°C-4110s (D). The label Y signifies the presence, while N indicates the absence, of the characteristic FTIR peaks.

FTIR bands of PANI	FTIR bands of N–C samples	A	B	C	D
	α – stretching of nitrile groups	Y	Y	Y	Y
a (1740 cm^{-1}) – stretching of –C═O– groups	**β** – stretching of sp^2-hybridized C═C bonds of aromatic or hetero-aromatic carbon rings	Y	Y	Y	Y
b (1643 cm^{-1}) –banding of H_2O molecule					
c (1607 cm^{-1}) –bending vibration of –N–H–					
d (1563 cm^{-1}) –stretching of the Q units (Q═N–Q)					
e (1477 cm^{-1}) –stretching of the B units (B–NH–B)	**γ** – non-carbonized B–NH–B units of PANI	Y	Y	N	N
f (1408 cm^{-1}) –stretching of phenazine heterocycles					
g (1300 cm^{-1}) –stretching of –C–N– in the aromatic amine	**δ*** – stretching of –C–N– in the aromatic amine	Y	Y	N	N
h (1241 cm^{-1}) –stretching of –C–N– in polaron lattice (═N⁺H–)					
i (1130 cm^{-1}) –vibration of charged Q and B structures (Q═NH^+–B)	**δ**** – –C–H in-plane bending of aromatic or hetero-aromatic carbon rings/ vibration of –C–O– bond from ethers, hydroxyl and carboxyl groups	Y	Y	Y	Y
j (1010 cm^{-1}) –in-plane –C–H banding of benzene ring/ vibration of –C–O– bond from the ether, hydroxyl, and carboxyl groups					

presence of PANI in emeraldine base and salt forms, along with N-phenylphenazine structural units. All carbonized samples showed significant changes in the FTIR band profile compared to bare PANI. At around 2219 cm^{-1}, a new band, labeled as **α**, appeared in C-450W-70s, C-450°C-2610s, C-450W-140s, and C-700°C-4110s samples. This peak is attributed to stretching vibrations of nitrile groups (–C≡N–) formed from the opening of benzenoid (**B**) and quinoid (**Q**) PANI rings at high

temperatures [39,43]. In the range of 1750-900 cm^{-1}, PANI peaks transformed into three broad bands, labeled as β, γ, and δ, in C-450W-70s and C-450°C-2610s samples, while C-450W-140s and C-700°C-4110s samples exhibited only β and δ bands. These changes are consistent with PANI transformation into disordered carbonaceous structures with nitrogen (N) and oxygen (O) functional groups at mild and moderate carbonization temperatures, respectively [43,44].

The presence of the β peak suggests modification of the Q=N–Q PANI backbone into aromatic or heteroaromatic carbon rings in all analyzed samples [37]. However, the β peak appeared at lower wavenumbers (~1597 ± 1 cm^{-1}) with lower intensity in the MW-heated samples, compared to higher wavenumbers (~1610 ± 2 cm^{-1}) with higher intensity in the CONV-heated samples. These differences may be related to the non-identical presence of neighboring O (e.g., –C=O bonds) or N (C=N bonds) groups of sp^2-hybridized carbon atoms in C-450W-70s and C-450°C-2610s, as well as in C-450W-140s and C-700°C-4110s samples [45,46].

The presence of peak γ in C-450W-70s and C-450°C-2610s samples may be attributed to the existence of residual, non-carbonized B–NH–B units of PANI [37,47]. However, under moderate carbonization conditions, these units may transform into hetero-aromatic carbon structures with tertiary N or pyrrolic N groups. As a result, the flattening of peak γ and the broadening of peak β were observed in both C-450W-140s and C-700°C-4110s samples, and related to the vibration of pentagons (pyrrole ring), heptagons, and the semi-circle stretching of the aromatic or hetero-aromatic carbon rings [40,48].

A broadband δ with a long tail was observed in C-450W-70s, C-450°C-2610s, C-450W-140s, and C-700°C-4110s samples after modification of charged PANI species, such as Q=NH$^+$–B or polarons. Significant differences were observed in the shape and position of this peak between the MW- and CONV-heated samples. In C-450W-70s, two maxima with high intensity were observed at 1306 cm^{-1} (δ*) and 1247 cm^{-1} (δ**), while the latter peak was less pronounced in the C-450°C-2610s sample. Under moderate conditions, the δ band appeared as a broad singlet with high intensity at 1252 cm^{-1} in C-450W-140s and with lower intensity at 1275 cm^{-1} in C-700°C-4110s samples. These results may suggest a higher presence of the –C–N bond of aromatic amines (indicated by the intense δ* peak at ~1300 cm^{-1}) in samples carbonized under mild conditions compared to moderate. The increased vibrations in the 1275-1000 cm^{-1} range (δ** peak) in MW-heated samples, as opposed to CONV-heated ones, could indicate a higher concentration of hydroxyl, carboxyl, ether, epoxide, and ketone species in the former

samples [45,49]. However, further investigation is needed to confirm these findings by using complementary spectroscopic techniques.

3.2. Raman analysis of carbonized PANI samples

Raman spectroscopy complemented the FTIR analysis by providing insights into the chemical composition, particularly examining a graphitic level and structural defects in both MW- and CONV-heated PANI samples. Fig. 2a displays Raman spectra of carbonized samples exhibiting the highest spectral similarity. For mild carbonization conditions, the Raman analysis contradicted FTIR observations. Specifically, the characteristic **G** (graphitic) and **D** (disordered) bands were not clearly defined in the spectrum of C-450°C-2610s (see **Fig. S2**), in contrast to its paired C-450W-70s sample. Instead, the Raman spectrum of C-450W-70s showed more similarities with a sample carbonized at 500°C (C-500°C-2910s). These variations may be related to non-uniform carbonization conditions within the same sample. However, the Raman spectrum of C-450W-140s complemented that of C-700°C-4110s, consistent with FTIR findings.

The Raman spectra of both MW- and CONV-heated samples displayed a broad **G** band, which corresponds to the stretching vibration of sp^2-hybridized C=C bonds in hexagonal carbon rings [48,50,51]. This band appeared at slightly higher wavenumbers (**G** band at 1590 cm^{-1}) in C-450W-140s and C-700°C-4110s compared to C-450W-70s and C-500°C-2910s samples (**G** band at 1582 cm^{-1}). Similar observations have been noted in the samples carbonized at high temperatures in other studies, and attributed to the presence of larger aromatic clusters (with graphene-like domains) along with increased compressive strain between them [52]. The **D** band (1356 ± 1 cm^{-1}) in MW- and CONV-heated samples is related to the semicircle stretching of C=C bonds on hexagonal carbon rings, influenced by defects like edges, vacancies, heteroatoms, and non-hexagonal rings. Additionally, a Raman peak at 2216 cm^{-1} with low intensity was observed in the spectra of C-450W-70s, C-500°C-2910s, C-450W-140s, and C-700°C-4110s samples, suggesting the presence of nitrile groups, consistent with FTIR observations.

To accurately compare the levels of graphitic (I_G) and disordered structures (I_D) in the Raman spectra, deconvolution was performed using five Gaussian curves. An example of this deconvolution for the C-450W-140s sample is shown in Fig. 2b. In addition to the G and D bands, the deconvolution revealed three other bands: D3 at 1457 cm^{-1}, D4 at 1238 cm^{-1}, and D5 at 1116 cm^{-1}. The D3 band is associated with
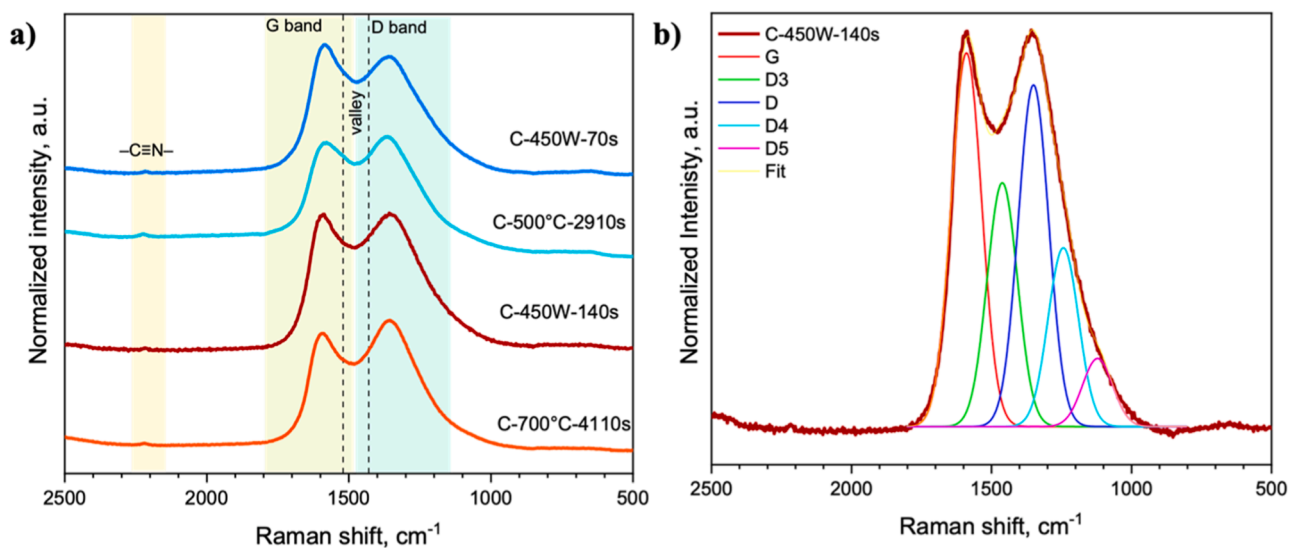

Fig. 2. (a) Raman spectra of MW- and CONV-heated samples show the highest spectral similarities. The comparison was made between C-450W-70s and C-500°C-2910s samples and between C-450W-140s and C-700°C-4110s samples. (b) deconvolution of the raw spectrum of the C-450W-140s sample.

vibrations caused by heteroatom defects and non-hexagonal ring systems [52]. The D4 and D5 bands are characterized by the secondary breathing modes of larger non-hexagonal rings containing heteroatoms, disrupted breathing modes of aromatic carbons with heteroatoms, and the fundamental breathing modes of small aromatic carbons [52]. Our results indicated that the intensity ratio I_D/I_G varied between 0.92 and 1.02 across the analyzed samples (see **Table S1**). Notably, the C-450W-140s and C-700°C-4050s samples displayed slightly lower I_D/I_G ratios, suggesting a higher level of graphitic order and, in turn, greater conductivity compared to the C-450W-70s and C-500°C-2910s samples.

In summary, Raman spectra confirmed the presence of disordered carbon structures with defects in the form of heteroatoms and non-hexagonal carbon rings in both MW- and CONV-heated samples. Raman analysis did not reveal significant variations in chemical composition between matched MW- and CONV- heated samples as observed in FTIR analysis, likely due to its lower sensitivity in distinguishing types of functional groups compared to FTIR. To further clarify the similarities in the functional groups between the analyzed samples, additional insights were obtained through XPS analysis.

3.3. XPS analysis of carbonized PANI samples

XPS analysis was used to compare the type and concentration of N and O functional groups in MW-heated samples with their respective samples in the CONV group by evaluating core-level spectra of nitrogen (N 1s, see **Fig. 3**), oxygen (O 1s, see **Fig. 4**) and carbon (C 1s, see **Fig. S3**) atoms. The typical types of N and O functional groups that could be found in carbon materials are illustrated in **Fig. S4**.

Analysis of N 1s core-level XPS spectra showed the highest similarities between C-450W-70s and C-450W-140s with C-500°C-2910s and C-700°C-4110s samples, respectively. **Fig. 3** displays five distinct peaks in the N 1s spectra of the analyzed samples: **N1** (397.8 ± 0.2 eV), **N2** (398.8 ± 0.2 eV), **N3** (399.9 ± 0.1 eV), **N4** (400.8 ± 0.1 eV), and **N5** (403.0 ± 0.1 eV). Minor variations of 0.1 eV in binding energy and below 11 % in peak area were observed in the N 1s spectra of C-450W-140s and C-700°C-4110s samples, suggesting very similar types and relative concentrations of N functional groups in these samples. In contrast, the C-450W-70s and C-500°C-2910s samples exhibited more pronounced variations, with changes reaching up to 0.3 eV in binding energy and up to 31 % (for **N1**) or 58 % (for **N4**) in peak areas. In general, both MW- and CONV-heated samples exhibited a mixture of N
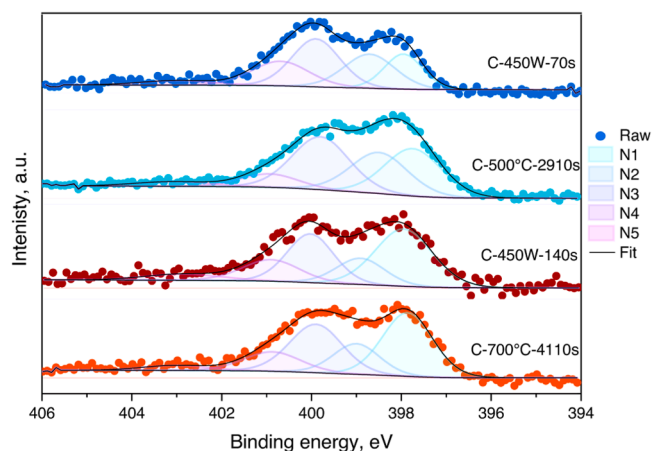
Fig. 3. N 1s core-level XPS spectra of MW- and CONV-heated samples show the highest spectral similarities. The comparison was made between C-450W-70s and C-500°C-2910s samples and between C-450W-140s and C-700°C-4110s samples. The peaks correspond to pyridinic N/imine functional groups (**N1**), primary and secondary amines/nitrile (**N2**), pyrrolic N/hydrogenated pyridinic N/tertiary amines (**N3**), tertiary amines (e.g. graphitic N) (**N4**) and shake-up signals (**N5**).
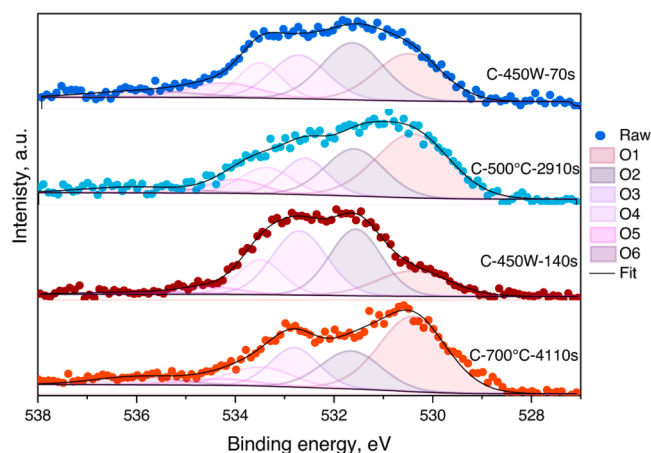
Fig. 4. O 1s core-level XPS spectra of MW- and CONV-heated samples show the highest spectral similarities. The comparison was made between C-450W-70s and C-500°C-2910s samples and between C-450W-140s and C-700°C-4110s samples. The peaks correspond to double-bonded O atoms in carbonyl and carboxyl groups (**O1**), epoxide/cyclic ether groups of lactones (**O2**), hydroxyl groups (**O3**), cyclic ether groups (**O4**), single-bonded O atoms in carboxyl or esters groups (**O5**) and moisture (**O6**).

functionalities, including pyridinic or imine functional groups (**N1**), primary and secondary amines or nitriles (**N2**), hydrogenated pyridinic or pyrrolic species (**N3**), graphitic N groups or tertiary amines surrounded by varying numbers of aromatic rings (**N4**) [53–58]. However, the relative amount of primary and secondary amines, or nitrile species (**N2** peak) was higher in the MW- and CONV- carbonized samples under mild than moderate conditions, consistent with FTIR findings. In contrast, pyridinic N (**N1** peak) formation was preferable at higher carbonization temperatures. The exact quantification of a single type of N species in MW- and CONV-heated samples is challenging to provide here, as the binding energies of N groups can overlap, influenced by factors such as the location of N atoms in the carbon plane (e.g., edge or basal), neighboring vacancy defects, or nearby functional groups (e.g., O-based) [53,54,59].

Fig. 4 presents the O 1s spectra of C-450W-70s, C-500°C-2910s, C-450W-140s, and C-700°C-4110s samples, emphasizing significant differences in spectral characteristics between these previously matched pairs. Six components were detected in the analyzed samples: **O1** (530.4 ± 0.1eV), **O2** (531.6 ± 0.1 eV), **O3** (532.7 ± 0.1 eV), **O4** (533.5 ± 0.1 eV), **O5** (534.3 ± 0.2 eV), and **O6** (535.9 ± 0.1 eV). While minor variations within 0.2 eV were observed in binding energies, notable differences were found in the relative areas of the detected O peaks. Particularly, significant variations were observed in **O1** (36 %) and **O3** peaks (31 %) for the C-450W-70s and C-500°C-2910s samples, while even greater differences were detected between the C-450W-140s and C-700°C-4110s samples, with variations of 61 % for **O1**, 38 % for **O2**, and 48 % for **O3** peaks. CONV-heated samples generally exhibited higher concentrations of double-bonded O atoms with C functionality, such as in carbonyl or carboxyl species (**O1** peak) [60–65]. In contrast, MW-heated samples showed increased levels of C–O–C groups of epoxy structures or aromatic ethers (**O2** peak), hydroxyl groups (**O3** peak), and cyclic ether groups found in compounds like pyrans, furans, and pyrenes (**O4** peak) [59,66–68]. MW- and CONV-heated samples demonstrated similar concentrations of single-bonded O atoms in carboxylic acid or ester groups (**O5** peak) [66], as well as moisture content (**O6** peak) [61]. The observed variations in the concentration of O functional groups between MW- and CONV-heated samples may be caused by the non-equivalent gas environment during the carbonization reaction [69] and the shorter reaction times for oxygen molecules to interact with the PANI backbone under rapid MW heating [70].

In summary, the observed variations in the position and intensity of

characteristic FTIR peaks in C-450W-140s and C-700°C-4110s samples could be associated with the identified differences in the levels of O functional groups, as N groups remained consistent across these samples. For instance, the higher concentration of carbonyl species (indicated by a high intensity of **O1**) in C-700°C-4110s resulted in a shift of the β peak to higher wavenumbers (~ 1610 cm^{-1}) and greater intensity compared to C-450W-140s, where the lower relative area of **O1** leads to a less intense β peak at ~ 1597 cm^{-1}. Similar trends have been observed previously [45,46]. The variations in the content of hydroxyls, epoxy, and cyclic ethers groups between C-450W-140s and C-700°C-4110s samples led to different intensity levels in the δ region of the FTIR spectra. Particularly, in C-450W-140s, with higher concentrations of these O functional groups, there was a stronger intensity of the δ peak in the 1200-1280 cm^{-1} range [71]. In contrast, C-700°C-4110s showed a lower content of hydroxyl, epoxy, and cyclic ether species (**O2, O3,** and **O4** peaks) and reduced intensity of the δ peak. Hence, these results showed that it is crucial to consider the influence of defects in carbon structures in the form of O functional groups on the resulting characteristic FTIR peaks, such as β and δ, during literature interpretation. Typically, these FTIR peaks have been analogously interpreted as peaks complementary with **G**-band-like (β) and **D**-band-like (δ) peaks in Raman spectra [39,43,72].

3.4. Electrocatalytic ORR performances of carbonized PANI samples

The ORR activity of the MW-heated sample was investigated and compared with the properties of the CONV-heated samples in alkaline media. The results revealed the greatest similarities in catalytic performance between the C-450W-70s and C-500°C-2910s samples, as well as between the C-450W-140s and C-700°C-4050s samples (see Fig. 5a). These conclusions were drawn after comparing the catalytic properties of these pairs with other CONV-heated samples at different temperatures (see **Fig. S5**). The C-450W-70s and C-500°C-2910s samples, carbonized under milder conditions, exhibited comparable onset potentials of 0.62 V versus a reversible hydrogen electrode (RHE), where the onset potential is defined as the potential at which a current density of 0.2 mA cm^{-2} is achieved. In contrast, the onset potentials for the C-450W-140s and C-700°C-4050s samples were 110 mV more positive than those carbonized under milder conditions. Furthermore, the diffusion-limited current densities of the C-450W-140s (-2.40 mA cm^{-2}) and C-700°C-4050s (-2.50 mA cm^{-2}) samples were significantly higher compared to the lower current density (-1.0 mA cm^{-2}) observed in the C-450W-70s and C-500°C-2910s samples at 0.5 V vs. RHE. The increase in ORR activity in samples carbonized under moderate conditions could be attributed to their enhanced graphitization level, which improves conductivity, and higher specific surface area (SSA), which hosts more active sites and enhances mass transport [16,73–75]. Specifically, for the MW-heated samples, the SSA increased from 236 m^2 g^{-1} in C-450W-70s to 522 m^2 g^{-1} in C-450W-140s. Similarly, for the CONV samples, the SSA increased from 398 m^2 g^{-1} in C-500°C-2910s to 524 m^2 g^{-1} in C-700°C-4050s. N$_2$ sorption analysis indicated type III adsorption isotherms (see **Fig. S8**) across all samples, suggesting macroporous architectures. Additionally, CO$_2$ sorption measurements confirmed the presence of ultramicropores within the analyzed materials. The reported SSA values of the analyzed materials are comparable to those found in the literature for PANI carbonized at similar temperature ranges [36, 76].

To further assess the efficiency of the catalysts, we calculated H$_2$O$_2$ selectivity using the RRDE method, based on measured disk current (I$_{disk}$) and ring current (I$_{ring}$). The highest I$_{ring}$ current, indicative of H$_2$O$_2$ oxidation on the Pt electrode, was observed between 0.4-0.5 V vs. RHE (refer to Fig. 5b). At the specific potential of 0.5 V vs. RHE, the H$_2$O$_2$ selectivity of the C-450W-70s, C-500°C-2910s, C-450W-140s, and C-700°C-4050s samples were similar, ranging between 79 % and 82 %. This similarity in H$_2$O$_2$ selectivity may indicate the catalytic sites governing the ORR to H$_2$O$_2$ are consistent across the samples, regardless of
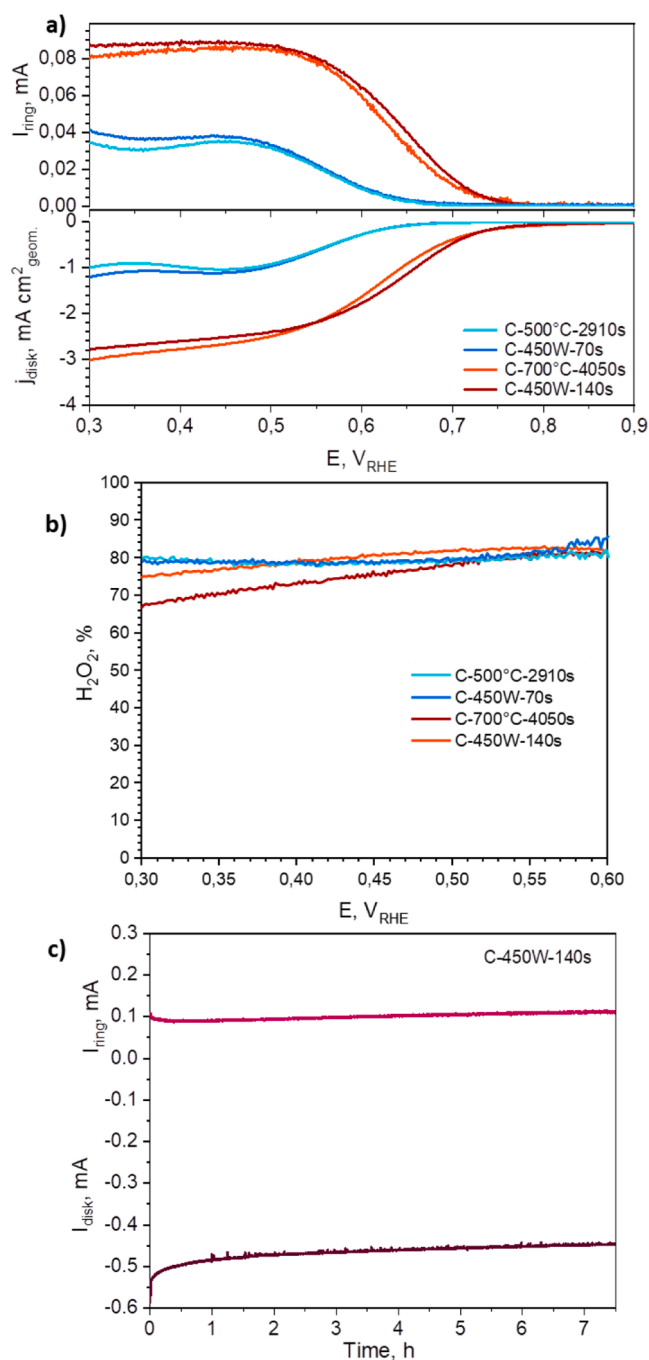
Fig. 5. (a) The LSV curves of MW- and CONV-heated samples that show the highest catalytic similarity in O$_2$-saturated 0.1 M KOH recorded at 1600 rpm and a scan rate of 10 mV s^{-1}. The comparison includes C-450W-70s versus C-500°C-2910s samples and C-450W-140s versus C-700°C-4110s samples. (b) H$_2$O$_2$ selectivity determined by RRDE method. (c) short-term stability tests of C-450W-140s at a potential of 0.5 V vs. RHE in O$_2$-saturated 0.1 M KOH.

their carbonization temperatures. XPS results showed a mixture of N functionalities in all samples, namely, C-450W-70s, C-500°C-2910s, C-450W-140s, and C-700°C-4050s (see Fig. 3). Notably, there was consistency in the relative concentration of hydrogenated pyridinic or pyrrolic species (N3) among these samples, while variations were observed in the relative concentration of pyridinic or imine functional groups (N1), primary and secondary amines or nitriles (N2), and graphitic N (N4). The literature still debates the exact roles of pyridinic N, graphitic N, and hydrogenated pyridinic or pyrrolic N species as active sites for ORR [4,15]. Some recent studies suggest that pyrrolic-N

appears to be the most important functional group for the catalysis of O_2 to H_2O_2 in alkaline media [15,26]. Even though our results show similar H_2O_2 yields across the tested samples, likely due to comparable concentrations of hydrogenated pyridinic or pyrrolic species, we believe that beyond the nitrogen functional groups, a well-developed and extensive pore network is crucial for preventing H_2O_2 trapping and achieving high selectivity. Further studies are needed to fully explore this complex and unresolved debate that is ongoing in the community.

Among the analyzed MW-heated samples (see **Fig. S6**), C-450W-140s showed the best overall electrocatalytic performance, demonstrating both high activity and selectivity. In contrast, low activity and low selectivity were observed in the C-450W-70s and C-450W-210s samples, respectively. Among the analyzed CONV-heated samples (see **Fig. S5**), C-700°C-4050s demonstrated the best ORR performance, which was analogous to that of the C-450W-140s sample. This similarity can be attributed to consistent structural characteristics reflected in the types of N functional groups (see Fig. 3) and to similar morphological features, as indicated by the consistent SSA (520 ± 4 m^2 g^{-1}) in both samples. Moreover, the scanning electron microscopy (SEM) images of both samples (**see Fig. S9**) reveal globular features with the presence of macropores. Despite these similarities, significant variations are observed in the O functional groups (see Fig. 4) between the C-450W-140s and C-700°C-4050s samples, which do not have a notable effect on H_2O_2 selectivity between the two samples. These results suggest that the mixed N groups could serve as the primary active sites for ORR to H_2O_2 in both C-450W-140s and C-700°C-4050s samples, while the O groups likely play a minor role. However, the role of O groups as active sites has been demonstrated in other studies mostly for carbon-based structures functionalized only with O groups, rather than in N, O-co-doped carbon [77–79]. Quinone groups are commonly classified as active sites for the ORR to H_2O_2, but other studies have also highlighted the potential roles of carboxyl groups at armchair edges, as well as epoxy or ring ether groups located on basal planes or at plane edges [15,80,81]. Similarly to nitrogen-based active sites, determining the exact nature of active sites within oxygen functional groups remains complex, especially when multiple heteroatoms are present in the carbon structure. This underscores the need for further systematic research to clarify these roles.

In addition to activity and selectivity, stability is another crucial factor for a catalyst's practical application. Thus, we assessed the stability of C-450W-140s, identified as the best-performing catalyst among the MW C-group, at a fixed potential of 0.5 V vs. RHE under the 7.5-hour chronoamperometry test. The currents recorded at both the ring and disk electrodes remained stable without significant decay during the test period (see Fig. 5c), indicating the good stability of the C-450W-140s catalyst. This is in agreement with the fact that metal-free catalysts possess a significant advantage in terms of stability compared to metal catalysts, attributed to the absence of metal dissolution degradation mechanisms, a known weakness of all metal-containing electrocatalysts [6,82]. Despite being widely used in the literature, we note that the RRDE may not be the best methodology to investigate the durability of the catalysts during 2e$^-$ ORR due to the limited oxygen solubility and mass transport, and thus lower H_2O_2 production rate. In our future work, we plan to devote more attention to investigating the activity, stability, and degradation mechanisms of carbon-based catalysts for electrochemical H_2O_2 synthesis using more appropriate setups, such as gas-diffusion electrode (GDE) [83,84].

The ORR performance of the C-450W-140s catalyst was evaluated against commercially available carbon materials, specifically Vulcan XC72 carbon black and KetjenBlack EC-600JD carbon black, as shown in **Fig. S10**. These commercial carbon materials contain heteroatoms, including oxygen, nitrogen, and sulfur, within their structure [85,86]. The C-450W-140s catalyst demonstrated comparable performance to Vulcan XC72 carbon black in terms of onset potential, diffusion-limiting current, and H_2O_2 selectivity. In comparison to KetjenBlack EC-600JD, the C-450W-140s catalyst exhibited a similar onset potential but achieved significantly higher H_2O_2 selectivity, with a value of 82 %

compared to 63 % for KetjenBlack EC-600JD at 0.5 V vs. RHE. These results suggest that the C-450W-140s catalyst performs similarly to, or even better than, well-established commercial benchmarks, highlighting its potential as an effective and sustainable alternative for H_2O_2 electrogeneration. Additionally, there is potential for further improvement of the C-450W-140s catalyst through targeted surface modifications.

Moreover, we also compared the C-450W-140s material with other catalysts reported in the literature that utilized MW heating. The results are summarized in Table 2. C-450W-140s showed the highest H_2O_2 production current and diffusion-limited current, surpassing values reported for other materials, indicating favorable catalytic activity. When the catalyst loading was reduced to 0.1 mg cm^{-2} (see LSV curves in **Fig. S7**) for equitable comparison, C-450W-140s exhibited competitive H_2O_2 selectivity of 90 % to literature data. Moreover, C-450W-140s also demonstrated comparable stability to literature reports. Overall, C-450W-140s showed similar or even superior ORR performance compared to other carbon-based catalysts utilizing MW heating. However, it should be underlined that most of the cited works primarily used MW heating for functionalization rather than synthesis itself for carbon-based catalysts. Specifically, they have investigated the modification of materials such as carbon nanotubes, graphene, and commercially available porous carbons. These precursors are initially formed through long multistep processes involving high-temperature treatments. Therefore, these synthesis approaches do not meet the sustainability criteria of short preparation time and energy non-invasiveness as seen in the preparation of C-450W-140s. As a result, C-450W-140s can be classified as a leading metal-free catalyst for H_2O_2 production where sustainable synthesis has been achieved.

4. Conclusion

The synthesis of metal-free heteroatom-doped carbon catalysts derived from PANI was demonstrated using a one-step MW-assisted heating approach under optimized conditions, namely, a power of 450 W and a heating time of 140 s (C-450W-140s sample). Mild and more severe degrees of carbonization were observed with a MW power of 450 W and a heating period of 70 and 210 s, respectively. FTIR, Raman, and XPS analyses confirmed the formation of nitrogen and oxygen-functionalized disordered carbon structures in the C-450W-140s sample. This sample exhibited a very similar distribution and concentration of carbon and nitrogen functionalities as the CONV carbonized samples, synthesized at 700°C for 4110 s (C-700°C-4110s). However, significant differences were observed in the oxygen functional groups, where the C-450W-140s sample displayed higher concentrations of hydroxyl, epoxy, and cyclic ether groups, and lower carbonyl content compared to the C-700°C-4110s sample. Despite these differences in chemical composition, both samples showed comparable electrocatalytic performances for ORR towards H_2O_2, including onset potential (0.73 ± 0.0 V vs. RHE), diffusion-limited current densities (-2.45 ± 0.05 mA cm^{-2}), and H_2O_2 selectivity (81 ± 1 %). These similarities can be attributed to nearly identical nitrogen functional groups and specific surface area in both samples, suggesting their role as major active sites. In summary, our study demonstrated a sustainable approach for synthesizing metal-free nitrogen-doped carbon catalysts with promising electrocatalytic properties, significantly reducing heating time by 29-fold and energy consumption by 77-fold compared to CONV methods.

CRediT authorship contribution statement

Milena Šetka: Writing – original draft, Visualization, Validation, Project administration, Funding acquisition, Formal analysis, Conceptualization. **Albert Behner:** Writing – original draft, Validation, Investigation. **Roman Bleha:** Investigation. **Milutin Smiljanić:** Writing – review & editing, Investigation. **Nejc Hodnik:** Writing – review & editing, Funding acquisition, Conceptualization. **Miroslav Šóóš:** Supervision, Funding acquisition.

Table 2

Comparison of the materials investigated in this work with literature data where MW heating was utilized for the preparation of carbon-based catalysts.

Material	Selectivity [a] %	j_{H2O2} [b] mA cm^{-2}	Diffusion-limited current* mA cm^{-2}	Duration of stability test h	Electrolyte	Loading mg cm^{-2}	Ref.
GN-rGO	63	1.2	-1.9	-	0.1 M KOH	0.1	[26]
Pyrr- rGO	95	2.4	-2.3	8	0.1 M KOH	0.1	[26]
GN-CNT	36	0.6	-2.3	-	0.1 M KOH	0.1	[26]
PyrrN-CNT	94	2.3	-1.9	8	0.1 M KOH	0.1	[26]
Mesoporous C	90	0.2#	-1.6	8	0.1 M KOH	-	[87]
C dots	92	1.6	-1.8	2.8	0.1 M KOH	-	[88]
C-450W-140s	82	2.9	-2.4	7.5	0.1 M KOH	0.2	This work
	90	3.6	-2.5	-	0.1 M KOH	0.1	

[a] Data is compared at 0.5 V vs. RHE. [b] j_{H2O2} is shown in mA. [j_{H2O2}] Data is calculated as I_{ring}/ N* $A_{geom.}$ [GN-rGO] Graphitic nitrogen doped-reduced graphene oxide. [PyrrN-rGO] Pyrrolic nitrogen doped-reduced graphene oxide. [GN-CNT] Graphitic nitrogen-doped carbon nanotubes. [PyrrN-CNT] Pyrrolic nitrogen-doped carbon nanotubes.

Declaration of competing interest

The authors declare that they have no known competing financial interests or personal relationships that could have appeared to influence the work reported in this paper.

Data availability

No data was used for the research described in the article.

Acknowledgments

Supplementary materials

Supplementary material associated with this article can be found, in the online version, at doi:10.1016/j.electacta.2024.145097.

References

[1] S. Yang, A. Verdaguer-Casadevall, L. Arnarson, L. Silvioli, V. Čolić, R. Frydendal, J. Rossmeisl, I. Chorkendorff, I.E.L. Stephens, Toward the decentralized electrochemical production of H2O2: a focus on the catalysis, ACS. Catal. 8 (2018) 4064–4081, https://doi.org/10.1021/acscatal.8b00217.

[2] S. Anantharaj, S. Pitchaimuthu, S. Noda, A review on recent developments in electrochemical hydrogen peroxide synthesis with a critical assessment of perspectives and strategies, Adv. Colloid Interface Sci. 287 (2021) 102331, https://doi.org/10.1016/j.cis.2020.102331.

[3] E. Lobyntseva, T. Kallio, N. Alexeyeva, K. Tammeveski, K. Kontturi, Electrochemical synthesis of hydrogen peroxide: Rotating disk electrode and fuel cell studies, Electrochim. Acta 52 (2007) 7262–7269, https://doi.org/10.1016/j.electacta.2007.05.076.

[4] M. Mazzucato, A. Facchin, M. Parnigotto, C. Durante, New and revised aspects of the electrochemical synthesis of hydrogen peroxide: from model electrocatalytic systems to scalable materials, ACS. Catal. (2024) 6369–6403, https://doi.org/10.1021/acscatal.4c01011.

[5] Y.Y. Jiang, P.J. Ni, C.X. Chen, Y.Z. Lu, P. Yang, B. Kong, A. Fisher, X. Wang, Selective electrochemical H2O2 production through two-electron oxygen electrochemistry, Adv. Energy. Mater. 8 (2018) 1801909, https://doi.org/10.1002/aenm.201801909.

[6] A.A. Topalov, I. Katsounaros, M. Auinger, S. Cherevko, J.C. Meier, S.O. Klemm, K.J. J. Mayrhofer, Dissolution of platinum: limits for the deployment of electrochemical energy conversion? Angew. Chemie Int. Ed. 51 (2012) 12613–12615, https://doi.org/10.1002/anie.201207256.

[7] C.H. Choi, C. Baldizzone, J.-P. Grote, A.K. Schuppert, F. Jaouen, K.J.J. Mayrhofer, Stability of Fe-N-C catalysts in acidic medium studied by operando spectroscopy, Angew. Chemie Int. Ed. 54 (2015) 12753–12757, https://doi.org/10.1002/anie.201504903.

[8] J.S. Choi, G.V Fortunato, D.C. Jung, J.C. Lourenço, M.R.V Lanza, M. Ledendecker, Catalyst durability in electrocatalytic H2O2 production: key factors and challenges, Nanoscale Horiz 9 (2024) 1250–1261, https://doi.org/10.1039/D4NH00109E.

[9] S. Cherevko, G.P. Keeley, S. Geiger, A.R. Zeradjanin, N. Hodnik, N. Kulyk, K.J. J. Mayrhofer, Dissolution of platinum in the operational range of fuel cells, ChemElectroChem 2 (2015) 1471–1478, https://doi.org/10.1002/celc.201500098.

[10] C. Zhang, W. Shen, K. Guo, M. Xiong, J. Zhang, X. Lu, A pentagonal defect-rich metal-free carbon electrocatalyst for boosting acidic O2 reduction to H2O2 production, J. Am. Chem. Soc. 145 (2023) 11589–11598, https://doi.org/10.1021/jacs.3c00689.

[11] Y. Sun, I. Sinev, W. Ju, A. Bergmann, S. Dresp, S. Kühl, C. Spöri, H. Schmies, H. Wang, D. Bernsmeier, B. Paul, R. Schmack, R. Kraehnert, B. Roldan Cuenya, P. Strasser, Efficient electrochemical hydrogen peroxide production from molecular oxygen on nitrogen-doped mesoporous carbon catalysts, ACS. Catal. 8 (2018) 2844–2856, https://doi.org/10.1021/acscatal.7b03464.

[12] I. Kruusenberg, J. Leis, M. Arulepp, K. Tammeveski, Oxygen reduction on carbon nanomaterial-modified glassy carbon electrodes in alkaline solution, J. Solid State Electrochem. 14 (2010) 1269–1277, https://doi.org/10.1007/s10008-009-0930-2.

[13] I. Palm, E. Kibena-Põldsepp, J. Lilloja, M. Käärik, A. Kikas, V. Kisand, M. Merisalu, A. Treshchalov, P. Paiste, J. Leis, A. Tamm, V. Sammelselg, K. Tammeveski, Impact of ball-milling of carbide-derived carbons on the generation of hydrogen peroxide via electroreduction of oxygen in alkaline media, J. Electroanal. Chem. 878 (2020) 114690, https://doi.org/10.1016/j.jelechem.2020.114690.

[14] Y.N. Ding, W. Zhou, J.H. Gao, F. Sun, G.B. Zhao, H2O2 electrogeneration from O2 electroreduction by N-doped carbon materials: a mini-review on preparation methods, selectivity of N sites, and prospects, Adv. Mater. Interfaces 8 (2021) 2002091, https://doi.org/10.1002/admi.202002091.

[15] M. Mazzucato, C. Durante, Insights on Oxygen reduction reaction to H2O2: The role of functional groups and textural properties on the activity and selectivity of doped carbon electrocatalysts, Curr. Opin. Electrochem. 35 (2022) 101051, https://doi.org/10.1016/j.coelec.2022.101051.

[16] M. Mazzucato, G. Daniel, V. Perazzolo, R. Brandiele, G.A. Rizzi, A.A. Isse, A. Gennaro, C. Durante, Mesoporosity and nitrogen doping: the leading effect in oxygen reduction reaction activity and selectivity at nitrogen-doped carbons prepared by using polyethylene oxide-block-polystyrene as a sacrificial template, Electrochem. Sci. Adv. 3 (2023) e2100203, https://doi.org/10.1002/elsa.202100203.

[17] J. An, Y. Feng, Q. Zhao, X. Wang, J. Liu, N. Li, Electrosynthesis of H2O2 through a two-electron oxygen reduction reaction by carbon based catalysts: From mechanism, catalyst design to electrode fabrication, Environ. Sci. Ecotechnol. 11 (2022) 100170, https://doi.org/10.1016/j.ese.2022.100170.

[18] E.S.F. Cardoso, G.V Fortunato, I. Palm, E. Kibena-Põldsepp, A.S. Greco, J.L. R. Júnior, A. Kikas, M. Merisalu, V. Kisand, V. Sammelselg, K. Tammeveski, G. Maia, Effects of N and O groups for oxygen reduction reaction on one- and two-dimensional carbonaceous materials, Electrochim. Acta 344 (2020) 136052, https://doi.org/10.1016/j.electacta.2020.136052.

[19] C. Xiong, Z. Wei, B. Hu, S. Chen, L. Li, L. Guo, W. Ding, X. Liu, W. Ji, X. Wang, Nitrogen-doped carbon nanotubes as catalysts for oxygen reduction reaction, J. Power. Sources 215 (2012) 216–220, https://doi.org/10.1016/j.jpowsour.2012.04.057.

[20] G. Panomsuwan, N. Saito, T. Ishizaki, Nitrogen-doped carbon nanoparticle–Carbon nanofiber composite as an efficient metal-free cathode catalyst for oxygen reduction reaction, ACS. Appl. Mater. Interfaces. 8 (2016) 6962–6971, https://doi.org/10.1021/acsami.5b10493.

[21] N. Yang, X. Zhu, G. Wang, L. Zhou, X. Zhu, J. Pan, W. Yu, C. Xia, C. Tian, Pyrolysis-free mechanochemical conversion of small organic molecules into metal-free heteroatom-doped mesoporous carbons for efficient electrosynthesis of hydrogen peroxide, ACS. Mater. Lett. 5 (2023) 379–387, https://doi.org/10.1021/acsmaterialslett.2c01005.

[22] H.J. Kitchen, S.R. Vallance, J.L. Kennedy, N. Tapia-Ruiz, L. Carassiti, A. Harrison, A.G. Whittaker, T.D. Drysdale, S.W. Kingman, D.H. Gregory, Modern microwave methods in solid-state inorganic materials chemistry: from fundamentals to manufacturing, Chem. Rev. 114 (2014) 1170–1206, https://doi.org/10.1021/cr4002353.

[23] S. Glowniak, B. Szczesniak, J. Choma, M. Jaroniec, Advances in microwave synthesis of nanoporous materials, Adv. Mater 33 (2021) 2103477, https://doi.org/10.1002/adma.202103477.

[24] K. Savaram, M.J. Li, K. Tajima, K. Takai, T. Hayashi, G. Hall, E. Garfunkel, V. Osipov, H.X. He, Dry microwave heating enables scalable fabrication of pristine holey graphene nanoplatelets and their catalysis in reductive hydrogen atom transfer reactions, Carbon 139 (2018) 861–871, https://doi.org/10.1016/j.carbon.2018.07.047.

[25] A.M. Schwenke, S. Hoeppener, U.S. Schubert, Synthesis and modification of carbon nanomaterials utilizing microwave heating, Adv. Mater. 27 (2015) 4113–4141, https://doi.org/10.1002/adma.201500472.

[26] J. Wan, G. Zhang, H. Jin, J. Wu, N. Zhang, B. Yao, K. Liu, M. Liu, T. Liu, L. Huang, Microwave-assisted synthesis of well-defined nitrogen doping configuration with high centrality in carbon to identify the active sites for electrochemical hydrogen peroxide production, Carbon 191 (2022) 340–349, https://doi.org/10.1016/j.carbon.2022.01.061.

[27] Q. Li, G. Fang, Z. Wu, J. Guo, Y. You, H. Jin, J. Wan, Advanced microwave strategies facilitate structural engineering for efficient electrocatalysis, ChemSusChem 17 (2024) e202301874, https://doi.org/10.1002/cssc.202301874.

[28] Y. Liu, T. Chen, T. Lu, Z. Sun, D.H.C. Chua, L. Pan, Nitrogen-doped porous carbon spheres for highly efficient capacitive deionization, Electrochim. Acta 158 (2015) 403–409, https://doi.org/10.1016/j.electacta.2015.01.179.

[29] N. Ishak, V. Jeyalakshmi, M. Setka, M. Grandcolas, B. Devadas, M. Šoóš, Upgrading of g-C3N4 semiconductor by a Nitrogen-doped carbon material: a photocatalytic degradation application, J. Environ. Chem. Eng. 11 (2023) 109381, https://doi.org/10.1016/j.jece.2023.109381.

[30] X. Xia, C.-F. Cheng, Y. Zhu, B.D. Vogt, Ultrafast microwave-assisted synthesis of highly nitrogen-doped ordered mesoporous carbon, Microporous Mesoporous Mater 310 (2021) 110639, https://doi.org/10.1016/j.micromeso.2020.110639.

[31] R. Kumar, S. Sahoo, E. Joanni, R.K. Singh, K.K. Kar, Microwave as a tool for synthesis of carbon-based electrodes for energy storage, ACS. Appl. Mater. Interfaces 14 (2022) 20306–20325, https://doi.org/10.1021/acsami.1c15934.

[32] J.J. Xu, R.F. Zhang, S.Y. Lu, H. Liu, Z.Y. Li, X.Y. Zhang, S.J. Ding, Ultrafast microwave-assisted synthesis of nitrogen-doped carbons as electrocatalysts for oxygen reduction reaction, Nanotechnology 29 (2018) 305708, https://doi.org/10.1088/1361-6528/aac3f5.

[33] J. Quílez-Bermejo, C. González-Gaitán, E. Morallón, D. Cazorla-Amorós, Effect of carbonization conditions of polyaniline on its catalytic activity towards ORR. Some insights about the nature of the active sites, Carbon 119 (2017) 62–71, https://doi.org/10.1016/j.carbon.2017.04.015.

[34] R. Silva, D. Voiry, M. Chhowalla, T. Asefa, Efficient metal-free electrocatalysts for oxygen reduction: polyaniline-derived N- and O-doped mesoporous carbons, J. Am. Chem. Soc. 135 (2013) 7823–7826, https://doi.org/10.1021/ja402450a.

[35] A.S. Varela, N.R. Sahraie, J. Steinberg, W. Ju, H.S. Oh, P. Strasser, Metal-doped nitrogenated carbon as an efficient catalyst for direct CO2 electroreduction to CO and hydrocarbons, Angew. Chemie Int. Ed. 54 (2015) 10758–10762, https://doi.org/10.1002/anie.201502099.

[36] S. Liu, Z. Zhang, F. Huang, Y. Liu, L. Feng, J. Jiang, L. Zhang, F. Qi, C. Liu, Carbonized polyaniline activated peroxymonosulfate (PMS) for phenol degradation: Role of PMS adsorption and singlet oxygen generation, Appl. Catal. B. 286 (2021) 119921, https://doi.org/10.1016/j.apcatb.2021.119921.

[37] S. Kuroki, Y. Hosaka, C. Yamauchi, A solid-state NMR study of the carbonization of polyaniline, Carbon 55 (2013) 160–167, https://doi.org/10.1016/j.carbon.2012.12.022.

[38] J. Hacaloglu, E. Argin, Z. Kücükyavuz, Characterization of polyaniline via pyrolysis mass spectrometry, J. Appl. Polym. Sci. 108 (2008) 400–405, https://doi.org/10.1002/app.27647.

[39] Z. Rozlívková, M. Trchová, M. Exnerová, J. Stejskal, The carbonization of granular polyaniline to produce nitrogen-containing carbon, Synth. Met. 161 (2011) 1122–1129, https://doi.org/10.1016/j.synthmet.2011.03.034.

[40] Z. Ping, In situ FTIR–attenuated total reflection spectroscopic investigations on the base–acid transitions of polyaniline. Base–acid transition in the emeraldine form of polyaniline, J. Chem. Soc., Faraday Trans. 92 (1996) 3063–3067, https://doi.org/10.1039/FT9969203063.

[41] G. Ćirić-Marjanović, Recent advances in polyaniline research: Polymerization mechanisms, structural aspects, properties and applications, Synth. Met. 177 (2013) 1–47, https://doi.org/10.1016/j.synthmet.2013.06.004.

[42] M. Trchová, J. Stejskal, Polyaniline: The infrared spectroscopy of conducting polymer nanotubes (IUPAC Technical Report), 83 (2011) 1803–1817. 10.1351/PAC-REP-10-02-01.

[43] M. Trchová, P. Matějka, J. Brodinová, A. Kalendová, J. Prokeš, J. Stejskal, Structural and conductivity changes during the pyrolysis of polyaniline base, Polym. Degrad. Stab. 91 (2006) 114–121, https://doi.org/10.1016/j.polymdegradstab.2005.04.022.

[44] M. Trchová, E.N. Konyushenko, J. Stejskal, J. Kovářová, G. Ćirić-Marjanović, The conversion of polyaniline nanotubes to nitrogen-containing carbon nanotubes and their comparison with multi-walled carbon nanotubes, Polym. Degrad. Stab. 94 (2009) 929–938, https://doi.org/10.1016/j.polymdegradstab.2009.03.001.

[45] M. Acik, G. Lee, C. Mattevi, A. Pirkle, R.M. Wallace, M. Chhowalla, K. Cho, Y. Chabal, The role of oxygen during thermal reduction of graphene oxide studied by infrared absorption spectroscopy, J. Phys. Chem. C115 (2011) 19761–19781, https://doi.org/10.1021/jp2052618.

[46] G.T.T. Le, J. Manyam, P. Opaprakasit, N. Chanlek, N. Grisdanurak, P. Sreearunothai, Divergent mechanisms for thermal reduction of graphene oxide and their highly different ion affinities, Diam. Relat. Mater. 89 (2018) 246–256, https://doi.org/10.1016/j.diamond.2018.09.006.

[47] M. Trchová, Z. Morávková, M. Bláha, J. Stejskal, Raman spectroscopy of polyaniline and oligoaniline thin films, Electrochim. Acta 122 (2014) 28–38, https://doi.org/10.1016/j.electacta.2013.10.133.

[48] Y. Yamada, H. Tanaka, Y. Tanaka, S. Kubo, T. Taguchi, S. Sato, Toward strategical bottom-up synthesis of carbon materials with exceptionally high pyridinic-nitrogen content: development of screening techniques, Carbon 198 (2022) 411–434, https://doi.org/10.1016/j.carbon.2022.06.069.

[49] P. Larkin, Infrared and Raman Spectroscopy: Principles and Spectral Interpretation, Elsevier Science, 2011.

[50] I. Kuno, A. Sato, S. Gohda, S. Sato, Y. Yamada, Bottom-up synthesis of carbon materials with an exceptionally high percentage of pentagons or tertiary nitrogen by brominating precursors, Carbon 213 (2023) 118188, https://doi.org/10.1016/j.carbon.2023.118188.

[51] D.B. Schüpfer, F. Badaczewski, J. Peilstöcker, J.M. Guerra-Castro, H. Shim, S. Firoozabadi, A. Beyer, K. Volz, V. Presser, C. Heiliger, B. Smarsly, P.J. Klar, Monitoring the thermally induced transition from sp3-hybridized into sp2-hybridized carbons, Carbon 172 (2021) 214–227, https://doi.org/10.1016/j.carbon.2020.09.063.

[52] M. Ayiania, E. Weiss-Hortala, M. Smith, J.-S. McEwen, M. Garcia-Perez, Microstructural analysis of nitrogen-doped char by Raman spectroscopy: Raman shift analysis from first principles, Carbon 167 (2020) 559–574, https://doi.org/10.1016/j.carbon.2020.05.055.

[53] Y. Yamada, H. Tanaka, S. Kubo, S. Sato, Unveiling bonding states and roles of edges in nitrogen-doped graphene nanoribbon by X-ray photoelectron spectroscopy, Carbon 185 (2021) 342–367, https://doi.org/10.1016/j.carbon.2021.08.085.

[54] T. Kato, Y. Yamada, Y. Nishikawa, T. Otomo, H. Sato, S. Sato, Origins of peaks of graphitic and pyrrolic nitrogen in N1s X-ray photoelectron spectra of carbon materials: quaternary nitrogen, tertiary amine, or secondary amine? J. Mater. Sci. 56 (2021) 15798–15811, https://doi.org/10.1007/s10853-021-06283-5.

[55] P. Lazar, R. Mach, M. Otyepka, Spectroscopic fingerprints of graphitic, pyrrolic, pyridinic, and chemisorbed nitrogen in N-doped graphene, J. Phys. Chem. C 123 (2019) 10695–10702, https://doi.org/10.1021/acs.jpcc.9b02163.

[56] M. Ayiania, M. Smith, A.J.R. Hensley, L. Scudiero, J.-S. McEwen, M. Garcia-Perez, Deconvoluting the XPS spectra for nitrogen-doped chars: an analysis from first principles, Carbon 162 (2020) 528–544, https://doi.org/10.1016/j.carbon.2020.02.065.

[57] M.J. Dzara, K. Artyushkova, S. Shulda, M.B. Strand, C. Ngo, E.J. Crumlin, T. Gennett, S. Pylypenko, Characterization of complex interactions at the gas–solid interface with in situ spectroscopy: the case of nitrogen-functionalized carbon, J. Phys. Chem. C 123 (2019) 9074–9086, https://doi.org/10.1021/acs.jpcc.9b00487.

[58] M. Figueras, I.J. Villar-Garcia, F. Viñes, C. Sousa, V.A. de la Peña O'Shea, F. Illas, Correcting flaws in the assignment of nitrogen chemical environments in N-doped graphene, J. Phys. Chem. C 123 (2019) 11319–11327, https://doi.org/10.1021/acs.jpcc.9b02554.

[59] T. Kato, Y. Yamada, Y. Nishikawa, H. Ishikawa, S. Sato, Carbonization mechanisms of polyimide: methodology to analyze carbon materials with nitrogen, oxygen, pentagons, and heptagons, Carbon 178 (2021) 58–80, https://doi.org/10.1016/j.carbon.2021.02.090.

[60] Y. Yamada, H. Yasuda, K. Murota, M. Nakamura, T. Sodesawa, S. Sato, Analysis of heat-treated graphite oxide by X-ray photoelectron spectroscopy, J. Mater. Sci. 48 (2013) 8171–8198, https://doi.org/10.1007/s10853-013-7630-0.

[61] M. Smith, L. Scudiero, J. Espinal, J.-S. McEwen, M. Garcia-Perez, Improving the deconvolution and interpretation of XPS spectra from chars by ab initio calculations, Carbon 110 (2016) 155–171, https://doi.org/10.1016/j.carbon.2016.09.012.

[62] R. Larciprete, P. Lacovig, S. Gardonio, A. Baraldi, S. Lizzit, Atomic oxygen on graphite: chemical characterization and thermal reduction, J. Phys. Chem. C 116 (2012) 9900–9908, https://doi.org/10.1021/jp2098153.

[63] A. Ganguly, S. Sharma, P. Papakonstantinou, J. Hamilton, Probing the thermal deoxygenation of graphene oxide using high-resolution In Situ X-ray-based spectroscopies, J. Phys. Chem. C 115 (2011) 17009–17019, https://doi.org/10.1021/jp203741y.

[64] J.-H. Zhou, Z.-J. Sui, J. Zhu, P. Li, D. Chen, Y.-C. Dai, W.-K. Yuan, Characterization of surface oxygen complexes on carbon nanofibers by TPD, XPS and FT-IR, Carbon 45 (2007) 785–796, https://doi.org/10.1016/j.carbon.2006.11.019.

[65] J. Zhou, P. Yang, P.A. Kots, M. Cohen, Y. Chen, C.M. Quinn, M.D. de Mello, J. Anibal Boscoboinik, W.J. Shaw, S. Caratzoulas, W. Zheng, D.G. Vlachos, Tuning the reactivity of carbon surfaces with oxygen-containing functional groups, Nat. Commun. 14 (2023) 2293, https://doi.org/10.1038/s41467-023-37962-3.

[66] A. Aarva, V.L. Deringer, S. Sainio, T. Laurila, M.A. Caro, Understanding X-ray spectroscopy of carbonaceous materials by combining experiments, density functional theory, and machine learning. Part I: fingerprint spectra, Chem. Mater. 31 (2019) 9243–9255, https://doi.org/10.1021/acs.chemmater.9b02049.

[67] A. Barinov, O.B. Malcioğlu, S. Fabris, T. Sun, L. Gregoratti, M. Dalmiglio, M. Kiskinova, Initial stages of oxidation on graphitic surfaces: photoemission study and density functional theory calculations, J. Phys. Chem. C 113 (2009) 9009–9013, https://doi.org/10.1021/jp902051d.

[68] A. Aarva, S. Sainio, V.L. Deringer, M.A. Caro, T. Laurila, X-ray spectroscopy fingerprints of pristine and functionalized graphene, J. Phys. Chem. C 125 (2021) 18234–18246, https://doi.org/10.1021/acs.jpcc.1c03238.

[69] C. Qiu, L. Jiang, Y. Gao, L. Sheng, Effects of oxygen-containing functional groups on carbon materials in supercapacitors: a review, Mater. Des. 230 (2023) 111952, https://doi.org/10.1016/j.matdes.2023.111952.

[70] X. Zhang, S.K. Manohar, Microwave synthesis of nanocarbons from conducting polymers, Chem. Commun. (2006) 2477–2479, https://doi.org/10.1039/B603925A.

[71] A. Bagri, C. Mattevi, M. Acik, Y.J. Chabal, M. Chhowalla, V.B. Shenoy, Structural evolution during the reduction of chemically derived graphene oxide, Nat. Chem. 2 (2010) 581–587, https://doi.org/10.1038/nchem.686.

[72] C. Russo, F. Stanzione, A. Tregrossi, A. Ciajolo, Infrared spectroscopy of some carbon-based materials relevant in combustion: qualitative and quantitative analysis of hydrogen, Carbon 74 (2014) 127–138, https://doi.org/10.1016/j.carbon.2014.03.014.

[73] D. Eisenberg, P. Prinsen, N.J. Geels, W. Stroek, N. Yan, B. Hua, J.-L. Luo, G. Rothenberg, The evolution of hierarchical porosity in self-templated nitrogen-doped carbons and its effect on oxygen reduction electrocatalysis, RSC. Adv. 6 (2016) 80398–80407, https://doi.org/10.1039/C6RA16606G.

[74] H. Xu, X.-H. Lv, H.-Y. Wang, J.-Y. Ye, J. Yuan, Y.-C. Wang, Z.-Y. Zhou, S.-G. Sun, Impact of pore structure on two-electron oxygen reduction reaction in nitrogen-doped carbon materials: rotating ring-disk electrode vs, Flow Cell, ChemSusChem 15 (2022) e202102587, https://doi.org/10.1002/cssc.202102587.

[75] Y. Sun, S. Li, B. Paul, L. Han, P. Strasser, Highly efficient electrochemical production of hydrogen peroxide over nitrogen and phosphorus dual-doped carbon nanosheet in alkaline medium, J. Electroanal. Chem. 896 (2021) 115197, https://doi.org/10.1016/j.jelechem.2021.115197.

[76] E.M. Kutorglo, J. Kovačovič, D. Trunov, F. Hassouna, A. Fučíková, D. Kopecký, I. Sedlářová, M. Šoóš, Preparation of carbon-based monolithic CO2 adsorbents with hierarchical pore structure, Chem. Eng. J. 388 (2020) 124308, https://doi.org/10.1016/j.cej.2020.124308.

[77] Z. Lu, G. Chen, S. Siahrostami, Z. Chen, K. Liu, J. Xie, L. Liao, T. Wu, D. Lin, Y. Liu, T.F. Jaramillo, J.K. Nørskov, Y. Cui, High-efficiency oxygen reduction to hydrogen peroxide catalysed by oxidized carbon materials, Nat. Catal. 1 (2018) 156–162, https://doi.org/10.1038/s41929-017-0017-x.

[78] J. Lee, J.S. Lim, G. Yim, H. Jang, S.H. Joo, Y.J. Sa, Unveiling the cationic promotion effect of H2O2 electrosynthesis activity of O-doped carbons, ACS. Appl. Mater. Interfaces 13 (2021) 59904–59914, https://doi.org/10.1021/acsami.1c17727.

[79] S.Y. Chen, T. Luo, K.J. Chen, Y.Y. Lin, J.W. Fu, K. Liu, C. Cai, Q.Y. Wang, H.J.W. Li, X.Q. Li, J.H. Hu, H.M. Li, M.S. Zhu, M. Liu, Chemical identification of catalytically active sites on oxygen-doped carbon nanosheet to decipher the high activity for

[80] M. Kullapere, J.-M. Seinberg, U. Mäeorg, G. Maia, D.J. Schiffrin, K. Tammeveski, Electroreduction of oxygen on glassy carbon electrodes modified with in situ generated anthraquinone diazonium cations, Electrochim. Acta 54 (2009) 1961–1969, https://doi.org/10.1016/j.electacta.2008.08.054.

[81] A. Sarapuu, K. Helstein, K. Vaik, D.J. Schiffrin, K. Tammeveski, Electrocatalysis of oxygen reduction by quinones adsorbed on highly oriented pyrolytic graphite electrodes, Electrochim. Acta 55 (2010) 6376–6382, https://doi.org/10.1016/j.electacta.2010.06.055.

[82] A. Lončar, D. Escalera-López, S. Cherevko, N. Hodnik, Inter-relationships between oxygen evolution and iridium dissolution mechanisms, Angew. Chemie Int. Ed. 61 (2022) e202114437, https://doi.org/10.1002/anie.202114437.

[83] B. Xia, Q. Huang, K. Wu, L. Jiang, M. Li, L. Yu, S. Ding, Z. Nie, D. Hua, J. Duan, S. Chen, Dynamic gas-diffusion electrodes for oxygen electroreduction to hydrogen peroxide, AIChE J 69 (2023) e18022, https://doi.org/10.1002/aic.18022.

[84] M. Li, Z. Zhu, S. Yuan, L. Ji, T. Zhao, Y. Gao, H. Wang, Nitrogen and oxygen co-doped graphite felt gas diffusion electrodes for efficient hydrogen peroxide electrosynthesis, Mol. Catal. 541 (2023) 113076, https://doi.org/10.1016/j.mcat.2023.113076.

[85] M.H.M.T. Assumpção, R.F.B. De Souza, D.C. Rascio, J.C.M. Silva, M.L. Calegaro, I. Gaubeur, T.R.L.C. Paixão, P. Hammer, M.R.V. Lanza, M.C. Santos, A comparative study of the electrogeneration of hydrogen peroxide using vulcan and printex carbon supports, Carbon 49 (2011) 2842–2851, https://doi.org/10.1016/j.carbon.2011.03.014.

[86] V. Čolić, S. Yang, Z. Révay, I.E.L. Stephens, I. Chorkendorff, Carbon catalysts for electrochemical hydrogen peroxide production in acidic media, Electrochim. Acta 272 (2018) 192–202, https://doi.org/10.1016/j.electacta.2018.03.170.

[87] Y.-L. Wang, S.-S. Li, X.-H. Yang, G.-Y. Xu, Z.-C. Zhu, P. Chen, S.-Q. Li, One minute from pristine carbon to an electrocatalyst for hydrogen peroxide production, J. Mater. Chem. A. Mater. 7 (2019) 21329–21337, https://doi.org/10.1039/C9TA04788C.

[88] T.-N. Pham-Truong, T. Petenzi, C. Ranjan, H. Randriamahazaka, J. Ghilane, Microwave assisted synthesis of carbon dots in ionic liquid as metal free catalyst for highly selective production of hydrogen peroxide, Carbon 130 (2018) 544–552, https://doi.org/10.1016/j.carbon.2018.01.070.